29th Annual Workshop on
Mathematical Problems in Industry
Worcester Polytechnic Institute, June 17–21, 2013

Modeling of Abrasive WaterJet for Precision Machining

"CFD Modeling of Abrasive-Fluid Jet for Precision Machining of Most Materials from Macro to Micro Scales"
problem presented by
Dr. Peter H.-T. Liu
OMAX Corporation

Participants:

D. Brady
C. Breward
R. Cao
I. Christov
J. Gambino
A. Hungria
G. Miller
R.O. Moore
W. Pickering
C. Please
M. Polin
L. Rossi
D. Schwendeman
B. Tilley
Z. Wei
S. Xu

Summary Presentation given by D. Brady, W. Pickering, J. Gambino
Summary Report compiled by R.O. Moore

---

1 Introduction

The abrasive waterjet (AWJ) is one type of abrasive fluid jet used in precision machining. With AWJ, a high-pressure water stream passes through a diamond orifice into a mixing chamber. Abrasive particles are gravity-fed into the mixing chamber, which is at a slight vacuum to help facilitate flow. There they mix with the water jet and pass into the collimating, or focusing, tube and are accelerated to nearly the speed of the water jet. The mixed abrasive fluid then passes out of the collimating tube to the cutting surface. The diagram on the right of Figure 1 illustrates how the abrasive is introduced into the water jet.

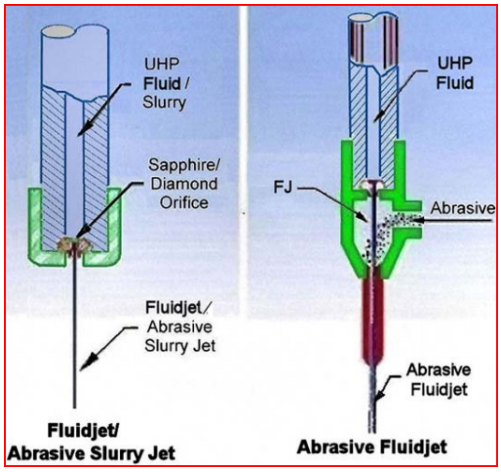

Figure 1: Schematic diagram of slurry and abrasive WaterJets

One problem with the abrasive waterjet is that there is a wide distribution in particle exit velocities. For a waterjet with an initial velocity of 700 m/s, particle exit velocities range from 200 – 600 m/s with an average velocity of 400m/s. This makes for less efficient cutting and is exacerbated by the presence of entrained air introduced at the mixing chamber.

Another issue depicted in Figure 2 is abrasive-induced wear in the collimating tube. This wear reduces the operational lifespan of the abrasive WaterJet.

Both of these issues are mitigated in the case of the slurry-based WaterJet, which has the advantage of not requiring a mixing chamber or collimating tube. This eliminates the problem of entrained air and removes the issue of wear in the collimating tube. At high pressures (approaching 600 MPa), however, the diamond orifice in the slurry-based WaterJet is worn down very quickly, effectively reducing the operational lifespan to a small fraction of the lifespan of the abrasive WaterJet. For this reason, the remainder of this report focuses on the abrasive WaterJet rather than on the slurry-based WaterJet.

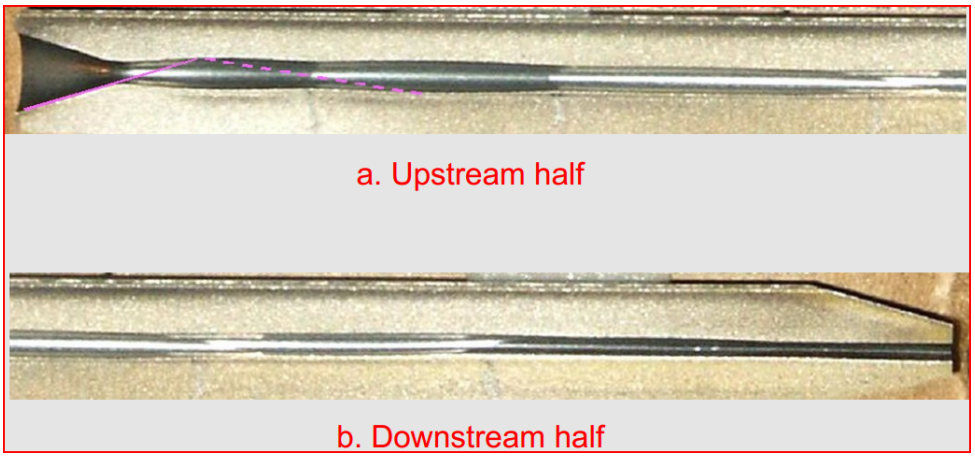

Figure 2: Collimating tube wear pattern.

2 Prior Work

Ye and Kovacevic [4] have modeled abrasive slurry jets using finite element methods and determined that particle size and nozzle geometry have a substantial impact on the number of times that a particle impacts the nozzle wall. They showed that both smaller particle size and a greater taper to the nozzle inlet reduced the number of impacts of a particle with the wall. Although their model looked at slurry jets instead of AWJ, the geometry of the slurry jet nozzle is similar to considering the bottom of the mixing chamber together with the collimating tube. In both cases, it appears that the nozzle geometry plays an important role in determining initial particle trajectory entering the tube and thus the number of subsequent impacts with the tube wall.

3 Models

In formulating the following models, we consider only the bottom region of the mixing chamber, at which the abrasive first interacts with the water jet, and the subsequent flow through the collimating tube. At $z = 0$, the water jet is moving at an initial velocity of 700 m/s and the particles are traveling at some small velocity, δ. The abrasive is assumed to be garnet particles, approximately 90 microns in diameter. The collimating tube diameter is three times the diameter of the particle, or 270 microns, and the water jet is initially twice the diameter of the particles, or 180 microns.

3.1 Continuum Model: Water and Air

Let us first examine the flow in the collimating tube without abrasive particles. Consider a nozzle of fixed radius R^* and of length $L \gg R^*$ in which an incompressible liquid of density $\rho^{(1)}$ flows concentrically through a compressible gas in the annulus with density $\rho^{(2)}$. We assume that the velocity in both the liquid and the jet is sufficiently large so that viscous effects in both fluid regions can be neglected. The interface $r^* = h^*(z^*, t^*)$ separates the liquid from the gas (we assume no gas diffusion in the liquid), and that the surface tension σ between the liquid and gas is constant.

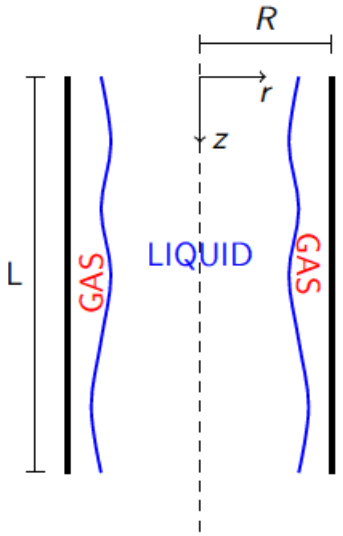

Figure 3: Geometry of water/air continuum model.

The equations of motion that describe the dynamics in the liquid are the incompressible Euler equations

$$\nabla \cdot \mathbf{u}^{(*1)} = 0 \,, \qquad (1)$$

$$\rho^{(1)} \left\{ \mathbf{u}^{(*1)}_{t^*} + \mathbf{u}^{(*1)} \cdot \nabla \mathbf{u}^{(*1)} \right\} + \nabla p^{(*1)} = 0 \,, \qquad (2)$$

where $\mathbf{u}^{(*1)} = u^{(*1)}(r^*, z^*, t^*)\mathbf{r} + w^{(*1)}(r^*, z^*, t^*)\mathbf{k}$ is the velocity in the liquid region $0 < r^* < h^*$, and $p^{(*1)}$ is the fluid pressure in the liquid jet. The gas dynamics in the annular region $h^* < r^* < R^*$ is governed by the compressible Euler equations and the equation of state, which for simplicity we model using

the ideal gas law

$$\rho^{(2)}_{t^*} + \nabla \cdot \left\{ \rho^{(2)} \, \mathbf{u}^{(*2)} \right\} = 0 \ , \tag{3}$$

$$\rho^{(2)} \left\{ \mathbf{u}^{(*2)}_{t^*} + \mathbf{u}^{(*2)} \cdot \nabla \mathbf{u}^{(*2)} \right\} + \nabla p^{(*2)} = 0 \ , \tag{4}$$

$$p^{(*2)} = R \rho^{(2)} T \ , \tag{5}$$

where $\mathbf{u}^{(*2)} = u^{(*2)}(r^*, z^*, t^*)\mathbf{r} + w^{(*2)}(r^*, z^*, t^*)\mathbf{k}$ is the velocity in the gas region $h^* < r^* < R^*$, and $p^{(*2)}$ is the gas pressure in the annulus.

Along the center of the nozzle, we assume symmetry conditions

$$r^* = 0 : \quad u^{(*1)} = 0 \ , \ \lim_{r^* \to 0} r^* w^{(*1)}_{r^*} = 0 \ , \tag{6}$$

and that the nozzle wall is impermeable to gas

$$r^* = R^* : \quad u^{(*2)} = 0 \ . \tag{7}$$

Along the free surface $r^* = h^*$, we require that the radial velocity is continuous, the jump in normal stress is balanced by capillary forces, and the kinematic boundary condition

$$u^{(*1)} = u^{(*2)} \ , \tag{8}$$

$$p^{(*1)} - p^{(*2)} = \sigma \left\{ \frac{1}{h^* \sqrt{1 + h^{*2}_{z^*}}} - \frac{h^*_{z^* z^*}}{\left(1 + h^{*2}_{z^*}\right)^{3/2}} \right\} \ , \tag{9}$$

$$h^*_{t^*} + w^{(*1)} h^*_{z^*} = u^{(*1)} \ . \tag{10}$$

We apply the following nondimensionalization to the variables

$$r = \frac{r^*}{R^*} \ , \ z = \frac{z^*}{L} \ , \ w^{(1,2)} = \frac{w^{(*1,*2)}}{W} \ , \ u^{(1,2)} = \frac{u^{(*1,*2)}}{U} \ , \ t = \frac{t^*}{L/W} \ , \ p^{(1,2)} = \frac{p^{(*1,*2)}}{\rho^{(1)} W^2} \ , \tag{11}$$

where $U = R^* W / L$ is the characteristic radial velocity, W is the characteristic axial velocity. In addition, we scale the gas density by the liquid density $\rho = \rho^{(2)} / \rho^{(1)}$ and the free surface on the nozzle radius $h = h^* / R^*$. With this scaling, the governing equations for the liquid are

$$\nabla \cdot \mathbf{u}^{(1)} = 0 \ , \tag{12}$$

$$\epsilon^2 \left\{ u^{(1)}_t + w^{(1)} u^{(1)}_z + u^{(1)} u^{(1)}_r \right\} + p^{(1)}_r = 0 \ , \tag{13}$$

$$w^{(1)}_t + u^{(1)} w^{(1)}_r + w^{(1)} w^{(1)}_z + p^{(1)}_z = 0 \ , \tag{14}$$

while in the gas

$$\rho_t + \nabla \cdot \left\{ \rho \, \mathbf{u}^{(2)} \right\} = 0 \ , \tag{15}$$

$$\epsilon^2 \left\{ u^{(2)}_t + w^{(2)} u^{(2)}_z + u^{(2)} u^{(2)}_r \right\} + \frac{1}{\rho} p^{(2)}_r = 0 \ , \tag{16}$$

$$w^{(2)}_t + u^{(2)} w^{(2)}_r + w^{(2)} w^{(2)}_z + \frac{1}{\rho} p^{(2)}_z = 0 \ , \tag{17}$$

$$p^{(2)} = \frac{c^2}{W^2} \rho \ , \tag{18}$$

where c is the speed of sound in the gas. We intend to apply a perturbation expansion in the aspect ratio $\epsilon = R^*/L \ll 1$ to determine the dominant equations of motion.

The homogeneous boundary conditions along the nozzle axis $r = 0$ and along the nozzle wall $r = 1$ remain unchanged, and along the free surface $r = h(z,t)$,

$$u^{(1)} = u^{(2)} \ , \tag{19}$$

$$p^{(1)} - p^{(2)} = We \left\{ \frac{1}{h\sqrt{1+\epsilon^2 h_z^2}} - \frac{\epsilon^2 h_{zz}}{(1+\epsilon^2\, h_z^2)^{3/2}} \right\} \ , \tag{20}$$

$$h_t + w^{(1)} h_z = u^{(1)} \ . \tag{21}$$

where $We = (\sigma/R^*)/(\rho_\ell W^2)$ is the Weber number of the flow. For the conditions for the water jet case, $We \approx 10$.

For the following, we assume that the flow in the annulus and in the jet is a plug flow, but the velocities need not be the same:

$$w^{(1)} = w^{(1)}(z,t) \ , w^{(2)} = w^{(2)}(z,t). \tag{22}$$

From the radial momentum equations (13), (16), we note that the pressure is independent of r, and we assume that the condition (20) defines the pressure difference to leading order. These assumptions lead to the following momentum equations for the jet and the annulus, in terms of the gas pressure $p^{(2)}$, where we retain only the axial component of capillarity in order to stabilize the numerical schemes later:

$$w_t^{(1)} + w^{(1)} w_z^{(1)} = p_z^{(2)} + We\, \frac{\partial}{\partial z} \left\{ \epsilon^2 h_{zz} - \frac{1}{h} \right\} \ , \tag{23}$$

$$w_t^{(2)} + w^{(2)} w_z^{(2)} + \frac{1}{\rho}\, p_z^{(2)} = 0. \tag{24}$$

We define the Mach number as $Ma = W^2/c^2 < 1$, and hence we have

$$Ma\, p^{(2)} = \rho \ . \tag{25}$$

To close the system, we need to solve for the radial velocity in each phase, and then require that all of the radial boundary conditions are satisfied. From the continuity equation (12), we find that

$$u^{(1)} = -\frac{r}{2}\, w_z^{(1)} \ , \tag{26}$$

while (15) provides a relation for $u^{(2)}$,

$$u^{(2)} = -\frac{r^2-1}{2r} \left\{ \frac{\rho_t + \left(\rho w^{(2)}\right)_z}{\rho} \right\} \ . \tag{27}$$

From (19) we find a relation for the gas density ρ

$$\rho_t + \left(\rho w^{(2)}\right)_z + \frac{h^2}{1-h^2} \rho w_z^{(1)} = 0. \tag{28}$$

Lastly, the kinematic boundary condition can be used with (26) to find

$$\left(h^2\right)_t + \left(h^2 w^{(1)}\right)_z = 0. \tag{29}$$

In principle, the nonlinear system of PDEs given by equations (23), (24), (28) and (29) can be integrated numerically to provide the dynamics of the water-air jet. Here we solve them with all time derivatives set to zero to find steady states, reducing the problem to four coupled ODEs. We can solve these easily using a numerical software package, e.g., MATHEMATICA.

The initial conditions used for all plots shown below are $w_1^{(0)} = 1$, $w_2^0 = \epsilon$, $h_0 = 0.5$, $\rho_0 = 10^{-3}$, $h'(0) = 0$, and $h''(0) = 1$. Figure 4 shows sample solutions for fixed Ma and ϵ and two different values for We. For large Weber number, surface tension becomes significant, which results in a wavier interface. Meanwhile, figure 5, shows solutions for fixed Ma, ϵ and We, using the same initial conditions as above (left) and using $h''(0) = 3$ (right). We observe the interface becoming increasingly wavy (specifically, larger amplitude and wavelength) with increasing initial curvature, suggesting these steady-state solution will be susceptible to Rayleigh–Plateau-type surface-tension-driven instabilities [1].

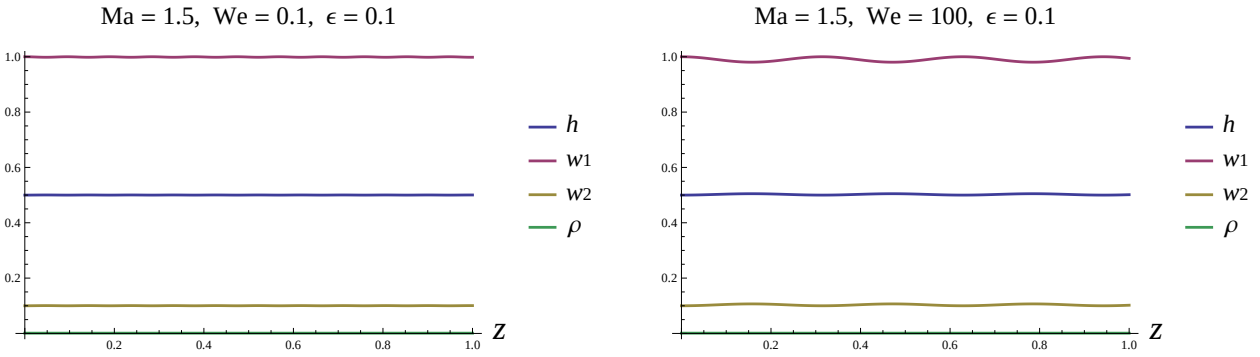

Figure 4: Steady-state solution of equations (23), (24), (28) and (29) for small (left) and large (right) Weber numbers.

Physical intuition would suggest that many or all of the above steady states are dynamically unstable. A comprehensive investigation of their stability is beyond the scope of this study, but it is straightforward to consider the *plug flow* case where the velocities, air density and jet radius are uniform in space. We linearize the governing equations about this solution to determine its stability to infinitesimal axial perturbations with wavenumber k. Substituting the ansatz

$$\begin{pmatrix} w^{(1)} \\ w^{(2)} \\ \rho \\ h \end{pmatrix}(z,t) = \begin{pmatrix} w_0^{(1)} \\ w_0^{(2)} \\ \rho_0 \\ h_0 \end{pmatrix} + \epsilon e^{\sigma t + ikz} \begin{pmatrix} \widetilde{w^{(1)}} \\ \widetilde{w^{(2)}} \\ \tilde{\rho} \\ \tilde{h} \end{pmatrix}, \tag{30}$$

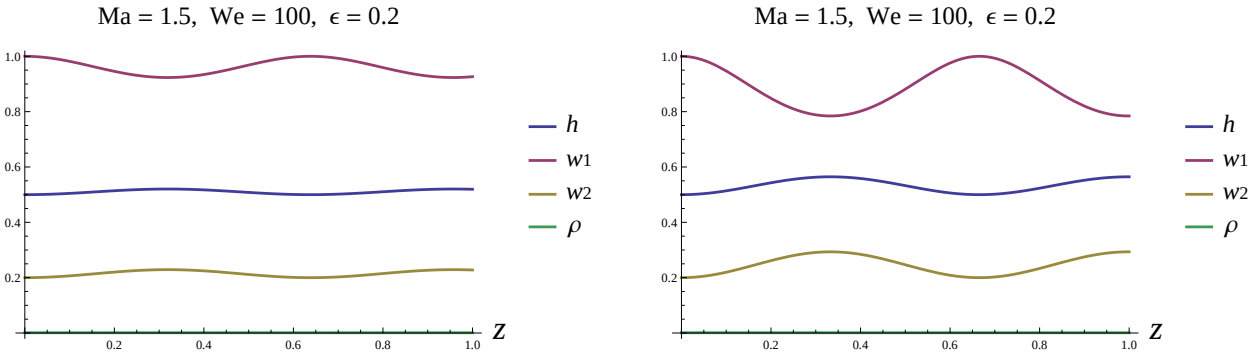

Figure 5: Steady-state solution of equations (23), (24), (28) and (29) for small initial curvature $h''(0) = 1$ (left) and large initial curvature $h''(0) = 3$ (right).

and keeping only leading order terms leads to the eigenvalue problem for the growth rate σ:

$$\begin{pmatrix} -ikw_0^{(1)} & 0 & \frac{ik}{Ma} & We\left(ikh_0 - i\epsilon^2 k^3\right) \\ 0 & -ikw_0^{(2)} & -\frac{ik}{\rho_0 Ma} & 0 \\ -\frac{ikh_0^2}{1-h_0^2}\rho_0 & -ik\rho_0 & -ikw_0^{(2)} & 0 \\ -\frac{ikh_0}{2} & 0 & 0 & -ikw_0^{(1)} \end{pmatrix} \begin{pmatrix} \widetilde{w^{(1)}} \\ \widetilde{w^{(2)}} \\ \tilde{\rho} \\ \tilde{h} \end{pmatrix} = \sigma \begin{pmatrix} \widetilde{w^{(1)}} \\ \widetilde{w^{(2)}} \\ \tilde{\rho} \\ \tilde{h} \end{pmatrix}. \tag{31}$$

The eigenvalues σ are determined by setting $\det(A - \sigma I) = 0$. Letting $\sigma = ikc$, $c_1 = c - w_0^{(1)}$ and $c_2 = c - w_0^{(2)}$, we arrive at the following algebraic equation relating k to c:

$$\frac{2c_1 c_2 h_0^2 \rho_0}{1 - h_0^2} = (1 - c_2^2 Ma)(2c_1^2 + We - \epsilon^2 We\, k^2 h_0). \tag{32}$$

Equation (32) is a quartic polynomial in c. We can analyze its roots (solutions to equation (32)) graphically as follows. The left-hand side is a quadratic polynomial in c with roots at $c_1 = 0$ and $c_2 = 0$, in other words, $c = w_0^{(1)}$ and $c = w_0^{(2)}$ (see figure 6). The right-hand side of equation (32) is a product of two quadratic polynomials in c. The roots of the first factor, $1 - c_2^2 Ma$, are easily seen to be $c_2 = \pm 1/\sqrt{Ma} \Rightarrow c = w_0^{(2)} \pm 1/\sqrt{Ma}$, which are both real. The roots of the second factor, $2c_1^2 + We - \epsilon^2 We\, k^2 h_0$, are $c_1 = \pm\sqrt{\frac{We}{2}(-1 + \epsilon^2 k^2 h_0)} \Rightarrow c = w_0^{(1)} \pm \sqrt{\frac{We}{2}(-1 + \epsilon^2 k^2 h_0)}$. The latter two roots are complex unless $\epsilon^2 k^2$ is sufficiently large. However, this model is derived in the *long-wavelength* (small k) approximation, hence we expect both ϵ and k to be small compared to $1 \Rightarrow \epsilon^2 k^2 \lll 1$. With this in mind, as figure 6 shows, there are only two intersections of the left- and right-hand sides of equation (32) for parameters relevant here. Hence, the quartic polynomial for c has two real roots. By the fundamental theorem of algebra, the other two roots are complex. Complex roots, meaning $\Im\{c\} \neq 0$ imply that $\Re\{\sigma\} \neq 0$ (by the definition of c). Therefore, the uniform plug flow base state is unstable for all k within the long-wavelength approximation. Physically, this implies that the high-speed water jet will eventually lose stability, even without abrasive particles present. Whether the plug flow loses stability to a different steady state or breaks up in a manner similar to the Rayleigh–Plateau instability [1] is beyond the scope of this document.

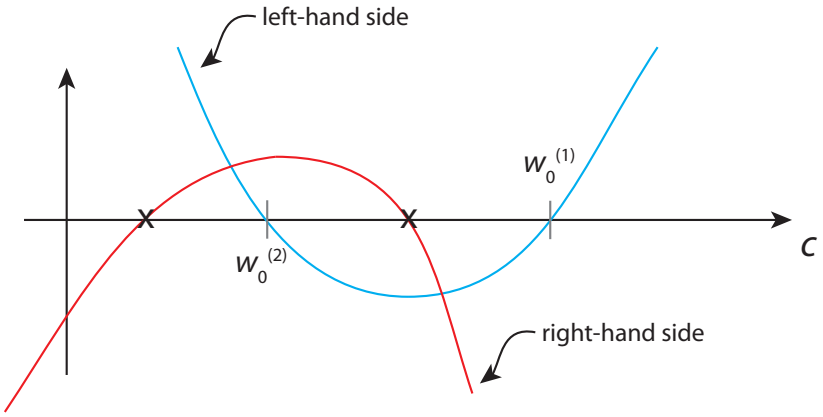

Figure 6: Graphical analysis of solutions of equation (32), showing that that quartic polynomial in c has only two real roots (intersections of the red and blue curve).

3.2 Continuum Model: Water and Particles

Next we consider the steady flow of water and particles in the collimating tube, neglecting the effects of air.

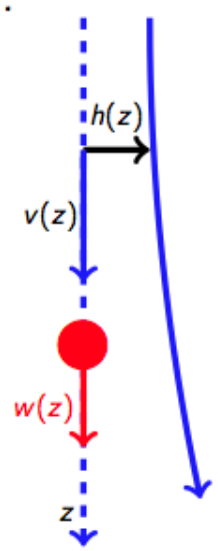

Figure 7: Geometry of water/particle continuum model.

Take $v(z)$ as the velocity of the fluid, $w(z)$ as the velocity of the particle, $h(z)$ as the radius of the cross section of the water jet, and $N(z)$ as the number of particles per unit length at position z. From conservation of mass and conservation of momentum of the particles and of the fluid, respectively, we have four equations:

$$\frac{d}{dz}\left(\rho v h^2\right) = 0, \tag{33}$$

$$\frac{d}{dz}(\bar{\rho} N w) = 0, \tag{34}$$

$$\frac{d}{dz}\left(\rho v^2 \pi h^2\right) = D_o N (w - v)|w - v|, \tag{35}$$

$$\frac{d}{dz}\left(\bar{\rho}\frac{4}{3}\pi a^3 N w^2\right) = -D_o N (w - v)|w - v|, \tag{36}$$

where ρ is the density of the fluid, $\bar{\rho}$ is the density of the particle ($4{\times}10^3$ kg/m^3), a is the radius of one particle (45μm), and D is the drag, defined by $D(N) = c_D \cdot \frac{1}{2}\rho \cdot (\pi a^2) \cdot N = D_o N$.

Our boundary conditions at $z = 0$ are given by

$$v(0) = v_0, \qquad w(0) = \delta \ll v_0, \qquad h(0) = h_0, \qquad N(0)w(0) = Q. \tag{37}$$

3.2.1 Non-dimensionlization

We define dimensionless variables

$$v = v_0\widehat{v}, \quad w = v_0\widehat{w}, \quad z = L\widehat{z}, \quad h = h_0\widehat{h}, \quad N = \frac{Q}{v_0}\widehat{N}, \tag{38}$$

where Q is a characteristic particle flux and L is a characteristic length defined by

$$L = \frac{2v_0h_0^2}{C_Da^2Q}.$$

This choice of scales introduces dimensionless parameter

$$\lambda = \frac{3}{4}\frac{v_0h_0^2}{a^3Q}\frac{\rho}{\bar{\rho}} \approx 10,$$

representing the mass flow rate of the liquid relative to that of the particles.

Dropping the hats and letting primes denote derivatives with respect to z, the dimensionless system is given by

$$\left(v\,h^2\right)' = 0, \tag{39}$$
$$\left(v^2\,h^2\right)' = N(w-v)|w-v|, \tag{40}$$
$$\left(Nw^2\right)' = -\lambda N(w-v)|w-v|, \tag{41}$$
$$(Nw)' = 0. \tag{42}$$

The boundary conditions are now

$$v(0) = 1, \qquad w(0) = \delta, \qquad h(0) = 1, \qquad \text{and} \qquad Nw(0) = 1. \tag{43}$$

From Equations (39) and (42), $vh^2 = 1$ and $Nw = 1$, so that Equations (40) & (41) become

$$v' = -N(v-w)|v-w| = -N(v-w)^2, \tag{44}$$
$$w' = \lambda N(v-w)|v-w| = \lambda(v-w)^2, \tag{45}$$

where we have assumed that $v \geq w$ throughout their evolution. The implicit solution to this initial value problem is

$$(1+\lambda)^2 z = \lambda \ln|v - \lambda(1-v) - \delta| + \frac{(\lambda+\delta)(1+\lambda)}{1-\delta}\left(\frac{1-v}{v-\lambda(1-v)-\delta}\right) - \lambda\ln|1-\delta|, \tag{46}$$
$$w = \lambda(1-v) + \delta. \tag{47}$$

As $\delta \to 0$ this solution approaches that depicted in Figure 8, where both v and w asymptote to $\lambda/(1+\lambda)$ as $z \to \infty$.

Using parameters $C_D = 1$, $v_0 = 750$ m/s, $a = 45$ μm, $\rho = 1$ g/mm, $\bar{\rho} = 4$ g/mm, and initial mass flow rates of 4 kg/min for the water and 0.4 kg/min for the abrasive, the characteristic length scale $L \approx 2$ mm over which the particle and fluid velocity (and jet radius h) reach equilibrium is very short relative to a typical collimating tube length of several centimetres. This is indicative of the fact that the length of the tube serves to collimate a beam that has already achieved liquid-particle momentum balance within a very short initial portion of the tube.

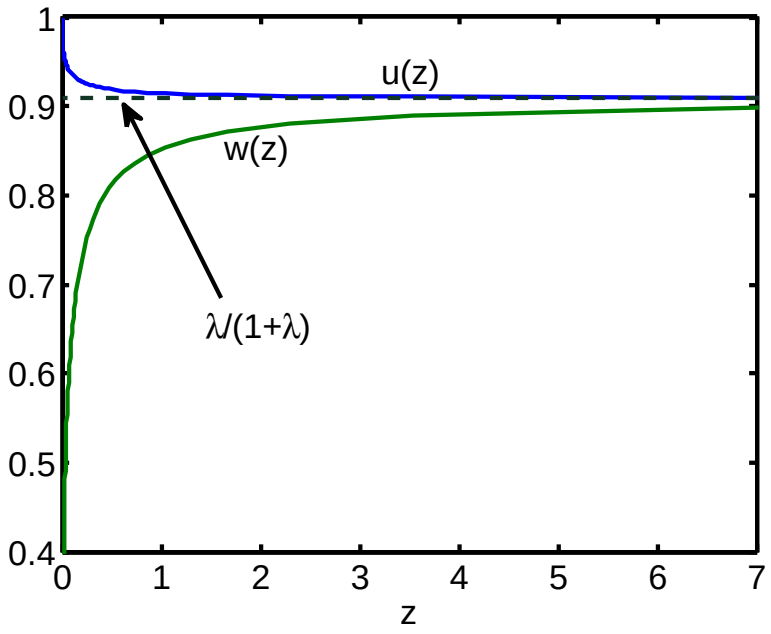

Figure 8: Water and particle velocities predicted by continuum model.

3.3 Continuum Model: Water, Air, and Particles

We now consider a three-phase flow of water, air, and abrasive particles. We again assume steady flow, i.e., with no time dependence. We assume water to be an inviscid, incompressible fluid and air to be an inviscid, compressible fluid.

	water	air	particles
volume fraction	α	β	$1-\alpha-\beta$
velocity	v_α	v_β	v_p
density	ρ_α	ρ_β	ρ_p
pressure	P_α	P_β	

By conservation of mass we have

$$\frac{d}{dz}\left(\rho_\alpha \alpha v_\alpha\right) = 0, \tag{48}$$

$$\frac{d}{dz}\left(\rho_\beta \beta v_\beta\right) = 0, \tag{49}$$

$$\frac{d}{dz}\left(\rho_p (1-\alpha-\beta) v_p\right) = 0, \tag{50}$$

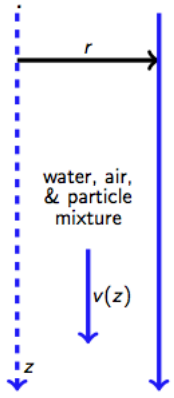

Figure 9: Geometry of three-phase continuum model.

and by conservation of momentum we have

$$\frac{d}{dz}\left(\rho_\alpha \alpha v_\alpha^2\right) = -\alpha \frac{dP_\alpha}{dz} - k_{\alpha\beta}\left(v_\alpha - v_\beta\right)^2 - k_{\alpha p}\left(v_\alpha - v_p\right)^2 - A\alpha v_\alpha^2, \tag{51}$$

$$\frac{d}{dz}\left(\rho_\beta \beta v_\beta^2\right) = -\beta \frac{dP_\beta}{dz} + k_{\alpha\beta}\left(v_\alpha - v_\beta\right)^2 - k_{\beta p}\left(v_\beta - v_p\right)^2 - B\beta v_\beta^2, \tag{52}$$

$$\frac{d}{dz}\left(\rho_p (1-\alpha-\beta) v_p^2\right) = k_{\alpha p}\left(v_\alpha - v_p\right)^2 + k_{\beta p}\left(v_\beta - v_p\right)^2 - C(1-\alpha-\beta) v_p^2. \tag{53}$$

To complete the system, we assume equations of state for the water and the air given by

$$P_\alpha = P_\beta, \qquad P_\beta = \rho_\beta RT. \tag{54}$$

The boundary conditions are given by

$$v_\alpha(0) = V_0, \quad v_\beta(0) = U_0, \quad v_p(0) = \delta Q, \tag{55}$$

$$\alpha(0) = \alpha_0, \quad \beta(0) = \beta_0, \quad P_\beta(0) = P_\alpha(0) = P_A - \frac{1}{2}\rho_\alpha U_0^2. \tag{56}$$

For this model, we assume that drag between the air and particles is negligible and that drag from the wall on the gas phase is negligible.

Then the reduced momentum equations are given by

$$\rho_\alpha V_0 v_\alpha' = -\alpha P' - k_{\alpha\beta}(v_\alpha - v_\beta)^2 - k_{\alpha p}(v_\alpha - v_p)^2 - A\alpha v_\alpha^2 \tag{57}$$

$$\beta_0 \rho_o U_0 v_\beta' = -\beta P' + k_{\alpha\beta}(v_\alpha - v_\beta)^2 \tag{58}$$

$$\rho_p(1-\alpha_0-\beta_0)\delta Q v_p' = k_{\alpha p}(v_\alpha - v_p)^2 - C(1-\alpha_0-\beta_0)\delta Q v_p \tag{59}$$

Numerical integration of these equations yields the plot of $v_p(1)$, the exit velocity of the particles, versus Q, the input particle flux, given in Figure 10. The corresponding experimental result is also shown. The numerically obtained curve can also be obtained analytically from the exact solution in equation (47) if the initial velocity $w(0)$ is allowed to depend on Q.

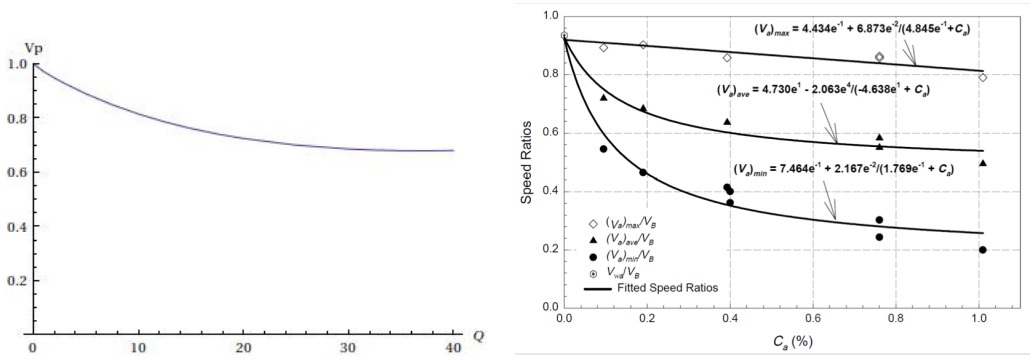

Figure 10: Numerically and experimentally obtained particle exit velocities, as a function of particle mass fraction.

3.4 Particle Dynamics: Basic Particle Model

The goal of these models is to follow the path of a single particle as it moves through the fluid, in order to explain the collimating tube damage depicted in Figure 2.

In these models we assume uniform fluid velocity and a fixed tube diameter. Particles are assumed to be spherical with some (nonzero) initial velocity. We begin by neglecting particle rotation.
Consider the movement of a spherical particle in a flow with fixed velocity through a pipe with length L. The pipe has radius a, the particle has radius r_0, the fluid has density ρ and the particle has density $\bar{\rho}$. The movement of the particle is modelled in dimensionless variables by:

$$\dot{r} = u, \tag{60}$$
$$\dot{u} = -k\|u - e_z v\|(u - e_z v), \tag{61}$$

where $k = \frac{2aC_D\rho}{3r_0\bar{\rho}}$. From the values described earlier for the particles and the fluid we find that $k \approx 1/16$. We model each collision with the wall as elastic with coefficient of restitution $C_r = .9$ and drag coefficient in the tangential direction $\mu = .01$. This yields the following "bounce" conditions when $|r \cdot e_x| = 1$:

$$u^+ \cdot e_x = -C_r u^- \cdot e_x, \tag{62}$$
$$u^+ \cdot e_z = u^- \cdot e_z - \mu\,(1 + C_r)\,u^- \cdot e_x, \tag{63}$$

where u^- is the velocity before the collision and u_+ is the velocity after the collision. We assume the particle is sliding down the incline on the side of the mixing chamber and entering the collimating tube with speed v_0. The initial conditions of this system are:

$$r_0 = \begin{pmatrix} r - 1 \\ 0 \end{pmatrix}, \tag{64}$$
$$u_0 = \begin{pmatrix} r|v_0|\cos\theta \\ |v_0|\sin\theta \end{pmatrix}, \tag{65}$$

where θ is angle the mixing chamber makes with the top of the collimating tube. We use $\theta = \pi/12$ for our numerical simulations. Using a value of $v_0 = .2$ we produce the trajectory shown in Figure 11. We then look at the points of impact along the wall associated with each bounce and their distribution for 1000 particles with initial velocity drawn from a normal distribution with mean $= .2$ and standard deviation .01. The distributions on the points along the wall associated with the impact are shown in Figures 12. These figures show that a small variance in initial velocity produces increasing variance in the impact points down the collimating tube. This is consistent with the observation in Figure 2 that the spread of impact points increases down the collimating tube.

3.5 Particle Dynamics: Wall Deformation

Knowing the particle trajectories through the collimating tube allows us to estimate the extent of wear at each point based on a momentum transfer calculation. We use the previous model of particles travelling through the collimating tube, drawing the initial velocities from a normal distribution meant to capture the spread of initial particle velocities induced by contact with the fluid in the mixing chamber. As before, we let $\tilde{k} = \frac{2aC_D\rho}{3r_0\bar{\rho}}$ in the equation of motion for the particle:

$$\ddot{r} = -\tilde{k}|\dot{r} - e_z|(\dot{r} - e_z).$$

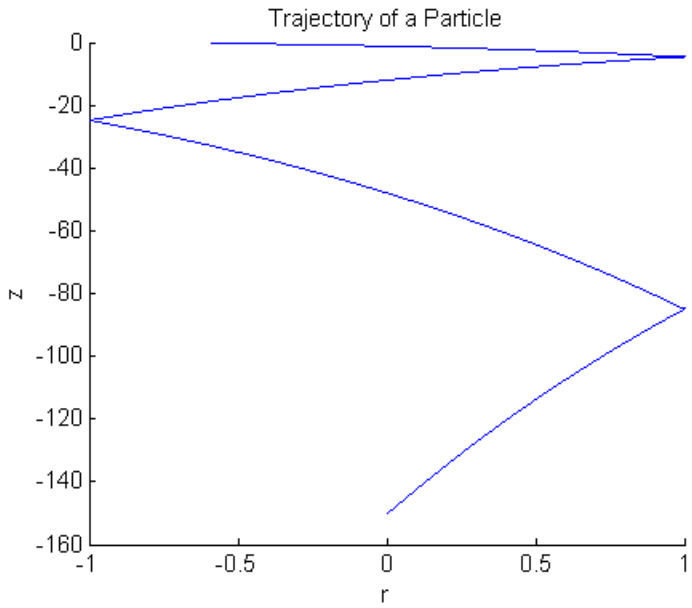

Figure 11: Particle trajectory in constant fluid flow.

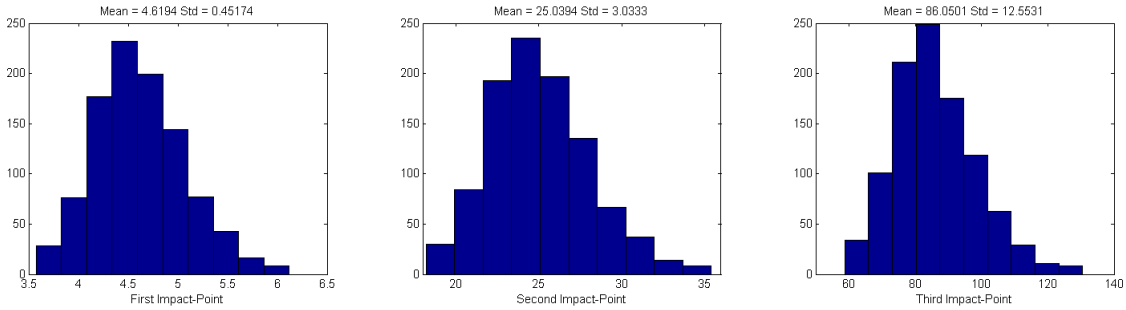

Figure 12: Histogram of first, second, and third impact sites along the z-axis.

We make the following assumptions for deformation of the walls. First, we assume that the deformation of the wall is small compared to the length of the tube. Second, we assume that the wall will only deform in the horizontal direction. Third, assume that the extent of wall deformation after being hit by a particle is proportional to the momentum absorbed by the wall. Recall that this was given by $-\mu(1 + C_R)|\dot{r} \cdot e_x|$.

Figure 13 shows a typical realization of this process. This single impact site is meant to represent the first wear "bulge" in Figure 2; subsequent local maxima in the wear pattern will occur further along the collimating tube consistent with the impact histograms shown in Figure 12.

3.6 Particle Dynamics: Considering Angular Momentum

In addition to considering the linear momentum of the particles, we can also consider the angular momentum for its effect on the collimating tube wear pattern and on the particle dynamics in the tube.
We assume the conditions of the previous model and that the particle is in contact with the wall

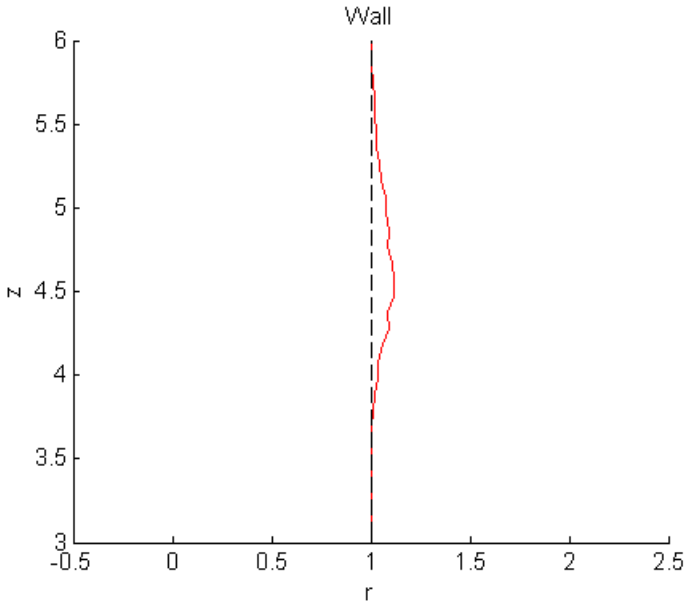

Figure 13: Wall shape at first impact site after Monte Carlo simulation.

for constant time δt during each collision. The tangential force τ delivered to the particle by the wall's impact is assumed proportional to the tangential velocity at the point of contact with the wall, $w_T - l\dot{\theta}$, yielding a change in angular momentum from hitting the wall given by

$$\Delta L = c(w_T - a\dot{\theta})l\delta t = cwa\delta t - ca^2\frac{L}{I}\delta t, \tag{66}$$

where I is the moment of inertia of the particle (given for spheres by $I = \frac{5ma^2}{2}$). If we then assume that the liquid has negligible effect on the particle's angular momentum between wall collisions, we have a recursive formula for finding the angular momentum L_k after bounce k:

$$L_{k+1} = L_k + \Delta L_k \tag{67}$$

$$= L_k + (-1)^k cwa\delta t - ca^2\frac{L_k}{I}\delta t \tag{68}$$

$$= \left(1 - ca^2\frac{\delta t}{I}\right) L_k + (-1)^k cwa\delta t. \tag{69}$$

Solving this difference equation with initial angular momentum L_0 gives

$$L_k = (-1)^k \left[m_0 \left(\frac{cl^2}{I}\delta t - 1 \right)^k + \frac{w_T a\delta t}{\frac{a^2}{I}\delta t - 2} \right] \quad \text{where} \quad m_0 = L_0 + \frac{cw_T l}{c\frac{a^2}{I}dt - 2}. \tag{70}$$

3.6.1 The Magnus Effect

The Magnus effect, depicted in the right diagram of Figure 14, is the lift provided by the pressure differential induced by a spinning ball moving through a fluid.

The lateral force exerted by the Magnus effect F_k is given by

$$F_k = S(L_k \times v), \tag{71}$$

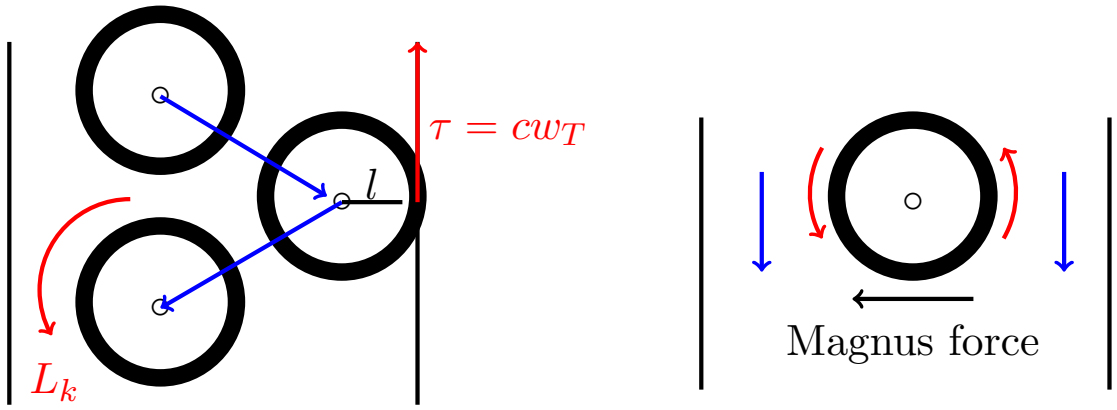

Figure 14: Angular momentum geometry (left) and Magnus effect (right).

where S is the angular drag coefficient. We include this in the lateral motion of the previous model, yielding the following adjusted equations:

$$\dot{r} = u, \tag{72}$$

$$\dot{u} = -k\|u - e_z v\|(u - e_z v) + \frac{F_k}{m}. \tag{73}$$

4 Conclusions

We have formulated several models in an endeavor to explain flow and wear patterns observed in the abrasive WaterJet. The first of these considers a high-speed jet of water (incompressible inviscid fluid to the leading order) surrounded by an annulus of air (compressible inviscid fluid to the leading order). To the leading order in the limit of small aspect ratio (long, thin jet), a high-speed water jet is a plug flow, which creates a plug flow in the surrounding air as well through the coupling of stresses at the jet's surface. A linear stability analysis of the spatially-uniform jet state shows that the plug is linearly unstable for all wavenumbers in the long-wavelength approximation. Since the governing equations are nonlinear, multiple steady-states are possible. Numerical solutions of nonuniform states are computed and shown to be "wavy" versions of the uniform base state, which are expected to be unstable as well, leading to the break up of the water jet under most conditions.

The second model includes water and a linear particle density to estimate momentum transfer between the two. It was seen through this model that equilibration occurs in a relatively short section of the collimating tube, to equilibrium velocities determined by the input mass flow ratio.

The third model represents three-phase flow and reaches similar conclusions to the water-particle model. Most importantly, it offers an explanation for the dependence of output particle velocity on

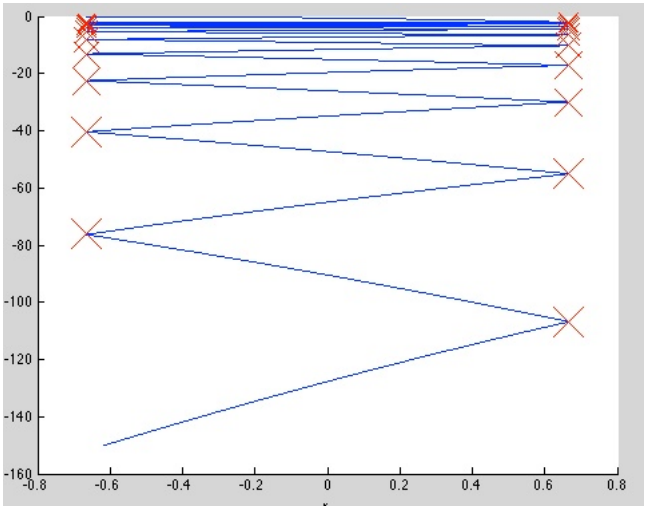

Figure 15: Sample particle trajectory including Magnus effect.

the initial particle mass flow rate.

Finally, atomistic models for the particles flowing in a known fluid velocity field appear to reproduce a distribution of wear consistent with that seen in experiment. The models suggest that it is important to include the impact of both linear and angular momentum to the collimating tube walls.

References

[1] P. G. Drazin and W. H. Reid. *Hydrodynamic Stability* (2nd ed). Cambridge, 2004.

[2] A. W. Momber and R. Kovacevic. *Priciples of Abrasive Water Jet Machining.* Springer, 1998.

[3] J. Wang. *Abrasive Water Jet Machining of Engineering Materials.* Trans Tech Publications, 2003.

[4] J. Ye and R. Kovacevic. Turbulent solid-liquid flow through the nozzle of premixed abrasive water jet cutting systems. *Proceedings of the Institution of Mechanical Engineers, Part B: Journal of Engineering Manufacture*, 213.1: 59-67, 1999.